JOURNAL OF COMPUTATIONAL PHYSICS **139,** 380–398 (1998)
ARTICLE NO. CP975870

An Adaptive Mesh Refinement Algorithm for the Radiative Transport Equation

J. Patrick Jessee,* Woodrow A. Fiveland,* Louis H. Howell,† Phillip Colella,† and Richard B. Pember†

* *Research and Development Division, Babcock & Wilcox, Alliance, Ohio 44601;* †*Center for Computational Sciences & Engineering, Lawrence Berkeley National Laboratory, Berkeley, California 94720*
E-mail: patrick.jessee@mcdermott.com

Received March 18, 1997; revised October 17, 1997

The discrete ordinates form of the radiative transport equation (RTE) is spatially discretized and solved using an adaptive mesh refinement (AMR) algorithm. This technique permits local grid refinement to minimize spatial discretization error of the RTE. An error estimator is applied to define regions for local grid refinement; overlapping refined grids are recursively placed in these regions; and the RTE is then solved over the entire domain. The procedure continues until the spatial discretization error has been reduced to a sufficient level. The following aspects of the algorithm are discussed: error estimation, grid generation, communication between refined levels, and solution sequencing. This initial formulation employs the step scheme and is valid for absorbing and isotropically scattering media in two-dimensional enclosures. The utility of the algorithm is tested by comparing the convergence characteristics and accuracy to those of the standard single-grid algorithm. For two simple benchmark problems, the AMR algorithm maintains the convergence characteristics of the standard single-grid algorithm, but it does not provide any efficiency gains due to a lack of disparate spatial scales. In a third, more localized problem, however, the AMR algorithm demonstrates significant memory and CPU time reductions.

Key Words: radiation; heat transfer; adaptive refinement.

1. INTRODUCTION

Most practical combustion applications exhibit a variety of length scales with some regions of the spatial domain containing much higher gradients than others. In addition, some applications involve moving fronts where the location and shape of the reaction zone change over time. To accurately predict the physical processes using a numerical model, the density of nodes or control volumes must be very high in the regions with steep gradients

0021-9991/98 $25.00

and may need to be spatially adapted over time to conform to the state of the fluid. Much progress has been made in the computational fluid dynamics community in developing spatial and temporal adaption algorithms to accurately predict the fluid dynamic processes with such disparate length and time scales [1–3].

In addition to convective and diffusive transport associated with fluid dynamics, radiative heat transfer often plays a large role in governing combustion dynamics. Radiative heat transfer is the dominant mode of heat transfer in many combustion applications and may significantly affect gas and wall temperatures. Because reaction rates and density distributions are closely linked to the local gas temperatures, radiative heat transfer may be very influential in combustion dynamics. Unfortunately, most deterministic methods for predicting radiative heat transfer have only been formulated for fixed computational grids which cannot support the locally refined grid structure necessary for resolving steep solution gradients and adapting to changing conditions. In this respect, the development of adaptive radiation techniques has largely lagged work in the computational fluid dynamics community.

For the prediction of multidimensional radiative heat transfer in participating media, the discrete ordinates (DO) method has been one of the most widely applied methods. It requires a single formulation to invoke higher order approximations, integrates easily into control volume transport codes, guarantees conservation of radiant energy, and is applicable to nongray [4] and anisotropically scattering media [5]. Based on these characteristics, the DO method has been selected for implementation into an adaptive mesh refinement environment.

The primary objective of this paper is to lay the foundation for applying the DO method in the context of spatial/temporal adaption. The methodology parallels the work of Bell *et al*. [1] for the compressible Navier–Stokes equations and is intended to complement the work being done at the Center for Computational Sciences & Engineering at Lawrence Berkeley National Laboratory. Methods outlined herein build on the existing software base for adaptive grid techniques and are compatible with the approach taken in the fluid dynamic development. The ultimate goal of the work is the incorporation of the present adaptive radiation algorithm in an unsteady, reacting flow solver. This paper represents the first step towards that goal; many of the benefits of the adaptive methods (especially runtime reduction) will be fully realized when unsteady, coupled physics applications are considered.

The remainder of the paper is broken into four sections. Section 2 presents the governing equations—the radiative transport equation and DO approximation. Section 3 details the adaptive mesh refinement (AMR) algorithm, while results from the algorithm are presented and discussed in Section 4. Finally, Section 5 summarizes the work and states conclusions based on the considered cases.

2. GOVERNING EQUATIONS

2.1. *Radiative Transport Equation*

This paper considers an emitting–absorbing and isotropically scattering gray medium, although the discrete ordinates method is not restricted to these conditions. For this medium, the radiative transport equation (RTE) is

$$(\Omega \cdot \nabla) I(\boldsymbol{r}, \Omega) = -(\kappa + \sigma) I(\boldsymbol{r}, \Omega) + \frac{\sigma}{4\pi} \int_{4\pi} I(\boldsymbol{r}, \Omega')\, d\Omega' + \kappa I_b(\boldsymbol{r}), \tag{1}$$

where $I(\boldsymbol{r}, \Omega)$ is the radiation intensity at position $\boldsymbol{r}$ and in direction Ω; $I_b(\boldsymbol{r})$ is the intensity of blackbody radiation at the temperature of the medium; and κ and σ are the gray absorption and scattering coefficients of the medium, respectively. This integro-differential equation, which governs the radiative heat transfer in a general spatial domain Λ, has both spatial and angular dependence.

For gray surfaces which reflect diffusely, the radiative boundary condition for Eq. (1) is given by

$$I(\boldsymbol{r}, \Omega) = \varepsilon I_b(\boldsymbol{r}) + \frac{\rho}{\pi} \int_{\boldsymbol{n}\cdot\Omega'<0} |\boldsymbol{n} \cdot \Omega'| I(\boldsymbol{r}, \Omega')\, d\Omega', \tag{2}$$

where $\boldsymbol{r}$ belongs to the domain boundary Γ and Eq. (2) applies for $\Omega \cdot \boldsymbol{n} > 0$, $I(\boldsymbol{r}, \Omega)$ is the intensity leaving a surface at a boundary condition location, ε is the surface emissivity, ρ is the surface reflectivity, and $\boldsymbol{n}$ is the unit normal vector at the boundary location.

2.2. *Discrete Ordinates Method*

The discrete ordinates method is a general method for solving the neutron or radiative transport equations. Only an overview will be given here since the method has been detailed elsewhere [6, 7]. The numerical solution of the RTE requires discretization of both spatial and angular domains. Formally, the discrete ordinates method only pertains to the angular discretization. Spatial and angular discretizations are typically performed independently, with the angular discretization performed first.

In the discrete ordinates method, the governing RTE is replaced by a discrete set of equations for a finite number of directions, Ω_m, and each integral is replaced by a quadrature,

$$(\Omega_m \cdot \nabla) I(\boldsymbol{r}, \Omega_m) = -\beta I(\boldsymbol{r}, \Omega_m) + \frac{\sigma}{4\pi} \sum_{k=1}^{M} w_k I(\boldsymbol{r}, \Omega_k) + \kappa I_b, \quad m = 1, \ldots, M, \tag{3}$$

where w_k are the ordinate weights. This angular approximation transforms the original integro-differential equation into a set of coupled differential equations. Weights and directions are commonly based on the S_n approximation [5, 8]. To simplify the presentation of the algorithm, the notation in Eq. (3) is simplified as

$$L_m(I_m) = \kappa I_b + S_m, \quad m = 1, \ldots, M, \tag{4}$$

where S_m denotes the in-scattering source term, and the operator L_m is defined as

$$L_m = (\Omega_m \cdot \nabla) + \beta. \tag{5}$$

After angular discretization has been performed, the DO equations may be discretized spatially using a number of techniques. Of the various techniques, the finite volume method (also known as the control volume method) is most widely used, principally because the method guarantees conservation of radiant energy, is computationally inexpensive, and is intuitively based. To reduce storage requirements, the transport equation for each ordinate

direction is usually discretized and solved independently. Inscattering source terms and reflected boundary conditions are updated through global iteration.

3. SOLUTION METHODS

3.1. *Adaptive Mesh Refinement (AMR) Algorithm*

The present algorithm focuses on solution of the steady-state RTE over a computational domain; the transient term of the RTE may be neglected for most practical problems as it is scaled by the inverse of the speed of light. Eventually, the algorithm is intended for integration into a transient, gas-phase combustion code which is based on the same grid structure and discretization methodology. Upon integration, the steady RTE calculations will be performed every time step, and coupling to the advective-diffusive energy transport equation will be considered. For coupled, transient calculations, regridding occurs at a prescribed time interval to track moving fronts of the developing flow field. The present algorithm for pure radiation calculations, which has stationary forcing functions (i.e. emissive power), differs from the transient algorithm in that grid adaption occurs after a complete solution to the RTE is obtained.

The development of the AMR algorithm for radiation transport follows the course taken by Bell *et al.* [1] for fluid dynamics. The governing equation are integrated (solved) over an hierarchial grid structure in which the grids have differing levels of refinement. The grid structure is based on an estimation of solution error; highly refined grids are placed in regions of the domain with relatively high spatial discretization error. The algorithm proceeds as follows: the discrete RTE is solved to some level of convergence on a given grid structure, an estimation of error is made, a new grid structure is generated, and the RTE is solved again. The process continues until the error has been reduced to a sufficient level.

Because the fluid dynamic and radiation modules are eventually intended to be closely coupled to perform combustion dynamics calculations, the grid structures for the two physics modules will most likely be the same. Generally, the distribution of local truncation error for the two modules, on which grid refinement is based, will not be the same due to the differing physical processes and to different variations in fluid dynamic and optical properties. Consequently, for coupled calculations a hybrid error estimator, which considers both fluid dynamic and radiative errors, will need to be developed. For pure radiation calculations presented in this paper, the local truncation error is estimated using gradients of the radiant intensity.

3.2. *Grid Structure and Nomenclature*

The grid structure may be characterized by a nested hierarchy of refined subgrids. The entire spatial domain is first covered by a set of disjoint grids of uniform refinement. A finer refinement level (defined by another set of grids) is then placed over the coarser level in locations where higher resolution is required. The finer set of grids is itself disjoint, but it need not be contiguous, and its resolution is described by an integral refinement ratio with respect to the coarse level. Fine grids may overlap more than one coarse grid and may be located adjacent to physical boundaries. Finer and finer refinement levels are recursively placed upon one another until the desired resolution is obtained. An example grid structure is shown in Fig. 1. The nesting procedure is detailed by Berger and Colella [9].

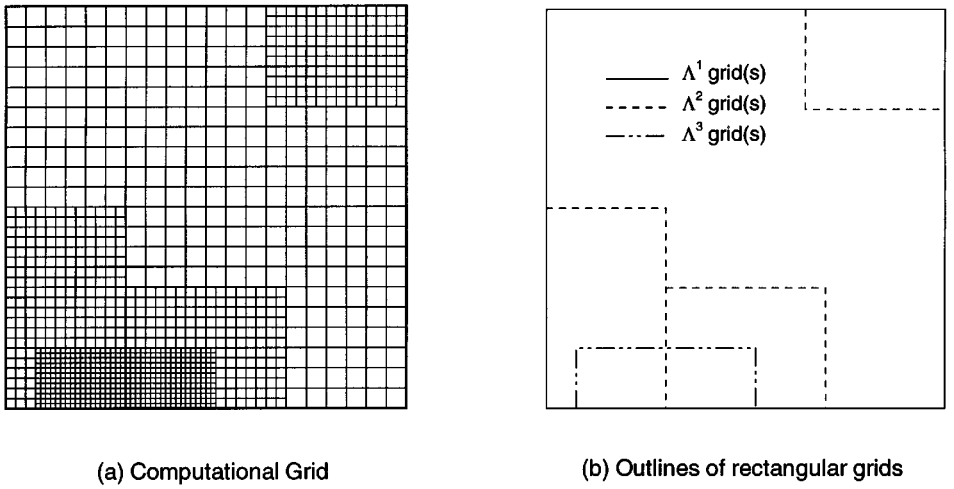

FIG. 1. Sample mesh hierarchy (two refinement levels).

The computational domain on a given level is denoted by the union of a disjoint set of rectangular grids,

$$\Lambda^l = \bigcup_{i=1}^{N^l} \Lambda_i^l, \tag{6}$$

where l and N^l are the level and the number of grids comprising the level, respectively. Portions of this domain may be covered by grids of a finer refinement level $(l+1)$. The area of overlap is defined by the projection of the finer level $(l+1)$ to the coarser (l) and is denoted by $\mathbf{P}(\Lambda^{l+1})$. The interior and exterior composite boundaries of the level are given by

$$\partial\Lambda^{l,\,in} = \bigcup_{i=1}^{N_l} \left(\partial\Lambda_i^l \bigcap_{j\neq i} \partial\Lambda_j^l \right) \tag{7}$$

$$\partial\Lambda^{l,e} = \left(\bigcup_{i=1}^{N^l} \partial\Lambda_i^l \right) - \partial\Lambda^{l,\,in} \tag{8}$$

where $\partial\Lambda_i^l$ represents the boundary of Λ_i^l. The interface between two levels of differing refinement (levels l and $l+1$) is represented by the exterior boundary of the finer level $(l+1)$. The projection of this interface to the coarser level is required for the communication between levels and is denoted by $\boldsymbol{P}(\partial\Lambda^{l+1,e})$.

3.3. *Single Grid Radiation Integrator*

The integration of the DO equations is based on standard finite volume techniques employed by Fiveland [5, 10], Fiveland and Jessee [11], and others. The radiation integrator is independent of the AMR shell, operating on single rectangular grids. When given a grid, suitable boundary conditions, and an ordinate direction by the AMR algorithm, the integrator solves an ordinate transport equation (Eq. (3)) over the rectangular patch. The integrator

only operates on a single ordinate direction rather than the entire set. The reason becomes clear when the composite grid algorithm is detailed.

The spatially discrete ordinate equation is obtained by integrating Eq. (3) over a typical control volume:

$$\frac{\mu_m}{\Delta x}(I_{m,i+1/2,j} - I_{m,i-1/2,j}) + \frac{\xi_m}{\Delta y}(I_{m,i,j+1/2} - I_{m,i,j-1/2}) = \kappa I_b - \beta I_{m,i,j} + S_m. \quad (9)$$

Similar equations may be written for all volumes within the single grid. Assuming given boundary, emission, and in-scattering conditions, the system of equations is closed by defining an interpolation scheme that relates the face intensities to the nodal values. Common approaches include the step, exponential, and diamond difference techniques. Because the exponential and diamond difference schemes are unbounded and often lead to oscillatory solutions, they are avoided in the present work, and the first-order step (upwind) scheme is exclusively applied. Although the step scheme is bounded, it has the disadvantage of being only first-order accurate. Since this paper is primarily concerned with algorithmic details and robustness of the methods, the use of the step scheme is appropriate. In practice, bounded, high resolution (HR) differencing schemes should be applied. Such schemes have recently been applied in a single-grid context by Fiveland and Jessee [11] and Jessee and Fiveland [12]. Future work will apply HR schemes to the current AMR algorithm.

For the step scheme, a given ordinate equation may be solved using a single sweep over the grid in which volumes are visited from upstream to downstream [10]. The process is analogous to ordering the equations from upstream to downstream to provide an upper triangular matrix and then back solving the system of equations. Multiple iterations are required to include the influence of in-scattering and wall reflections.

3.4. *Multiple-Level Algorithm*

The purpose of the multiple-level algorithm is to obtain a solution to the discrete RTE over the composite grid structure. This should not be confused with multigrid algorithms whose purpose is to accelerate solutions, although multigrid techniques may be used in conjunction with the present multiple-level algorithm. The multiple-level problem may be expressed as

$$L_m^l(I_m^l) = \kappa I_b^l + S_m^l \quad \text{on } \Lambda^l - \boldsymbol{P}(\Lambda^{l+1}) \quad (10)$$

$$I_m^l = \langle I_m^{l+1} \rangle \qquad \text{on } \boldsymbol{P}(\partial\Lambda^{l+1}),\ l < l_{\max} \quad (11)$$

for all m, where $\langle\cdot\rangle$ denotes a spatial averaging operator. These governing equations state that the RTE must be satisfied on any *uncovered* portion of the composite grid and the intensity field must be continuous at interfaces between levels of differing refinement—the flux leaving one portion of the computational domain must equal the flux entering the adjacent portion. This statement neglects the solution on a portion of any level that is *covered* by a level of finer refinement, namely in the region $\boldsymbol{P}(\Lambda^{l+1})$.

The present multiple-level algorithm is based on the approach of Bell *et al.* [1] and differs substantially from the standard single-level algorithm for the DO method [5, 10]. For a given ordinate direction, the standard solution algorithm sweeps the spatial grid from upstream to downstream. This approach may be extended to an embedded grid with the modifications that when a ray passes from a coarse to fine grid, the interface intensity is

interpolated, and when a ray passes from a fine to coarse grid, the interface intensity is averaged. One spatial sweep provides the composite solution to the ordinate equation over the composite grid. More sweeps would be required to include the influence of explicitly treated wall reflection and in-scattering terms. This approach has disadvantages from efficiency and programming standpoints. Because the interpolation and averaging operations are embedded in the sweep of the spatial grid, computation loops in the solution process are extremely small or are broken by conditional blocks of code. This not only limits the degree of vectorization and parallelization, but also it greatly increases the complexity of the coding.

The proposed multiple-level algorithm differs from the standard one in that levels in the grid hierarchy are operated on individually. For instance, in a two-level algorithm, the process begins by solving the RTE over the entire coarse level. Next the conditions at the coarse–fine interface are interpolated and applied to the boundary of the fine level, and the RTE is solved on this level. Fluxes leaving the fine level are then averaged and applied to the coarse grid to ensure conservation, and the coarse grid solution is again found, this time with the influence of the fine level. The transfer of information between levels is similar to the approach detailed by Bell *et al.* [1] and Berger and Colella [9]. At coarse-fine interfaces, intensities are interpolated with a piecewise constant operator, while averaging is performed using an area-weighted operator. Iteration between the levels continues until the composite solution is converged. This domain decomposition approach has the disadvantage that iteration between the levels is required. Nevertheless, present studies have shown that for cases with partially reflecting walls and/or scattering media, global convergence of the method is comparable to the single grid algorithm (see the Results, Section 4). The approach has the advantage that the sweeping, interpolation, and averaging operations are applied over large regions with uniformly spaced grids.

Formally, the multiple-level algorithm proceeds as follows:

- Compute emission and scattering sources on each level.
- Perform single space-angle sweep on coarsest level Λ^1.
- Transfer (interpolate) solution to boundary $\partial\Lambda^{2,e}$.
  - Perform single space-angle sweep on level Λ^2.
  - Transfer (interpolate) solution to boundary $\partial\Lambda^{3,e}$.

    $\vdots$

    - Perform single space-angle sweep on level Λ^{lmax}.
    - Average fluxes at downstream boundaries for coarser level.

    $\vdots$

  - Perform single space-angle sweep on level Λ^2.
  - Average fluxes at downstream boundaries for coarser level.
- Return to beginning of cycle if not converged.

On the first sweep of the coarse level, the coarse-fine interface is neglected since no information from the finer level is available at this time.

In general, the single space-angle sweep on a given level involves the solution on more than one rectangular grid. Special sequencing of the solution on the level is necessary to guarantee the efficient transfer of information across the domain. If the grids are not adjacent

to one another, the boundary conditions are established by either the coarser level conditions or by the physical boundary conditions, and sequencing is immaterial. However, if the grids are adjacent, the upstream conditions for one grid are provided from the downstream conditions of another. This dependence necessitates that the solution over the grids proceeds in an ordered fashion; the upstream grids must be swept first. Because the upstream direction varies with ordinate direction, different orderings are required for different ordinate directions. The number of unique orderings is 2^n, where n is the spatial dimension (e.g., $n = 2$ for two-dimensional space). The orderings correspond to the principal directions (e.g., all possible permutations of $(\pm 1, \pm 1)$ for two-dimensions) and may be denoted by the sets C_j^l, $j = 1, \ldots, 2^n$. Each set C_j^l contains a list of ordered grids for the particular principal direction. In addition, each ordinate direction may be assigned one of these ordered sets—a relationship denoted by the pointer $j(m)$—by inspecting the signs of the respective direction cosines. Whenever a new grid structure is generated, these grid orderings may be predetermined for each level. During the level space-angle sweep, the solution sequence first loops over ordinate directions and then over the ordered grids for the given direction:

For $m \in \{1, \ldots, M\}$ do
    For $i \in C_{j(m)}^l$ do
        • Obtain upstream boundary conditions from adjacent upstream grids on same level.
        • Solve ordinate equation m on grid i: $L_m^l(I_m^l) = \kappa I_b^l + S_m^l$ on Λ_i^l
    Enddo
Enddo

3.5. *Error Estimator*

The local truncation error (LTE) is measured by the normalized gradient of the radiant intensity,

$$LTE_m = \Delta x \frac{|\nabla I_m|}{I_m}, \tag{12}$$

where Δx denotes the characteristic cell size. To provide a single error estimator, an average LTE is defined

$$\overline{LTE} = \frac{1}{M} \sum_{m=1}^{M} LTE_m. \tag{13}$$

In the adaptive algorithm, the mesh is refined in portions of the domain where the inequality

$$\overline{LTE} > \theta \tag{14}$$

is satisfied, where θ is a user-specified error tolerance. The refinement criterion of Eq. (14) provides the ability to uniformly reduce the error (or estimate thereof) over the entire domain with no prior knowledge of the solution. The specific value of the error tolerance should be based on accuracy needs and may need to be determined from refinement studies on the given problem. The error estimator itself should be fairly accurate for the first-order step scheme, but will be overly conservative when high-order schemes are applied. For high-order differencing schemes, other estimators, such as one based on the finite volume analogue of the Zhu–Zienkiewicz estimator [13], will be more appropriate.

4. RESULTS

The radiation algorithm is investigated by considering two standard benchmark cases and a case to "simulate" a coupled transient analysis:

(1) Black rectangular enclosure with a purely absorbing medium
(2) Gray, rectangular enclosure with a purely scattering medium
(3) Black enclosure with a moving emission source.

The evaluation of the adaptive algorithm is based on the following criteria: (1) accuracy, (2) total computation time, and (3) convergence characteristics.

Results are compared to the exact solutions and predictions from other workers. Global energy balances are resolved to machine roundoff for the converged solutions. Convergence is measured by the normalized difference in the incident energy from two successive space-angle sweeps:

$$\|R\|_\infty = \max\{R_i : i = 1, \ldots, N_{\text{cell}}\} < 10^{-6}, \tag{15a}$$

where

$$R_i = \frac{\left|G_i^{n+1} - G_i^n\right|}{G_i^{n+1}} \tag{15b}$$

and superscripts n and i denote the iterate and cell index, respectively. The level-symmetric even S_6 ordinate set [8] was used for all cases unless otherwise indicated. A short description of the individual cases follows.

4.1. *Black Rectangular Enclosure with an Absorbing Medium*

The case consists of a two-dimensional, rectangular enclosure with cold walls and a purely absorbing medium maintained at an emissive power of unity [10, 11]. Absorption coefficients, κ, of 1 and 10 are individually considered.

For the case of black walls, spatially exact solutions to the S_n equations are available (see Appendix A). This is not the "exact" solution to the RTE, but the spatially exact solution to the angular approximation. Therefore, it may be used to measure the error due solely to a given spatial discretization (i.e., the computational mesh and spatial differencing order). Measurement of angular discretization error, namely ray effects, is another topic and should be considered separately. To quantify the spatial discretization (SD) error, the error definition is used,

$$E(x, y) = \frac{|G(x, y) - \bar{G}(x, y)}{G(x, y)} \times 100\%, \tag{16}$$

where $\bar{G}$ and G represent the spatially exact and approximate DO solutions, respectively. In addition, the following norms are defined:

$$\|E\|_1 = \frac{\sum V_i E_i}{\sum V_i} \tag{17}$$

$$\|E\|_\infty = \max\{E_i : i = 1, \ldots, N_{\text{cell}}\}. \tag{18}$$

The summations in Eq. (17) extend over all cells in the computational domain.

TABLE 1
Error and Timing Statistics for Case 1 ($\kappa = 1$)

Grid	$\|E\|_1$	$\|E\|_\infty$	CPU time (s)	No. of cells
10×10	3.140	13.34	0.13	100
20×20	2.041	11.29	0.43	400
40×40	1.201	7.296	1.68	1600
80×80	0.6775	4.073	6.91	6400
160×160	0.3718	2.280	28.34	25600
$\theta = 0.2$	1.891	5.154	38.49	2500 (4)[a]
$\theta = 0.1$	1.009	2.894	58.52	5396 (4)
$\theta = 0.05$	0.5813	2.024	102.61	11892 (4)
$\theta = 0.025$	0.3213	1.0983	309.17	48244 (5)

[a] Value in parentheses denotes final number of refinement levels.

Optical thicknesses of 1 and 10 were individually analyzed on uniform grids of 10×10, 20×20, 40×40, 80×80, and 160×160 and adaptive grids found with error tolerances (θ) of 0.2, 0.1, 0.05, and 0.025. The accuracy and timing results are shown in Table 1 for κ of 1. The table displays the two error norms, total CPU time, and the number of computational cells. For the adaptive analyses, the CPU time includes the time required for all refinement cycles, the number of cells corresponds to the mesh for the last refinement cycle, and the final number of refinement levels is shown in parentheses. The number of cells is displayed to quantify the memory requirements. All adaptive cases employ a refinement ratio of 2 for demonstration purposes, although the algorithm is implemented for a generic refinement ratio.

As expected, SD error is reduced as the grid resolution is increased. The adaptive algorithm is effective in reducing both the maximum and average error norms; however, the adaptive analyses generally require more CPU time than the uniform analyses with comparable error. Such undesirable behavior is due to a number of factors: several cycles are required for the adaptive algorithm to build up the refined mesh hierarchy; multiple iterations are required at each cycle to transfer information over the refinement levels; and lastly, the problem does not contain a wide range of length scales. The increase due to the first factor will be nonexistent during transient analyses because refinement is intertwined in the time-stepping procedure. The increase due to the second factor will be largely mitigated when either partially reflecting walls and/or scattering media are considered since the convergence on a given grid structure is generally governed by the explicitly treated reflection and scattering terms as will be shown later. The last factor will be less prevalent for more physical problems which do contain a range of length scales (e.g., more localized problems).

The ability of the adaptive algorithm to reduce memory requirements is shown in the last column of Table 1. The relative memory usage is be approximated by the total number of cells because the only persistent, noncell-based data structures are located at the edges of the fine grids (e.g., the coarse-fine interfaces) and are generally negligible, compared to the cell-based data structures. The comparison of the uniform 160×160 and adaptive $\theta = 0.05$ cases reveals that similar error norms are obtained with the adaptive algorithm

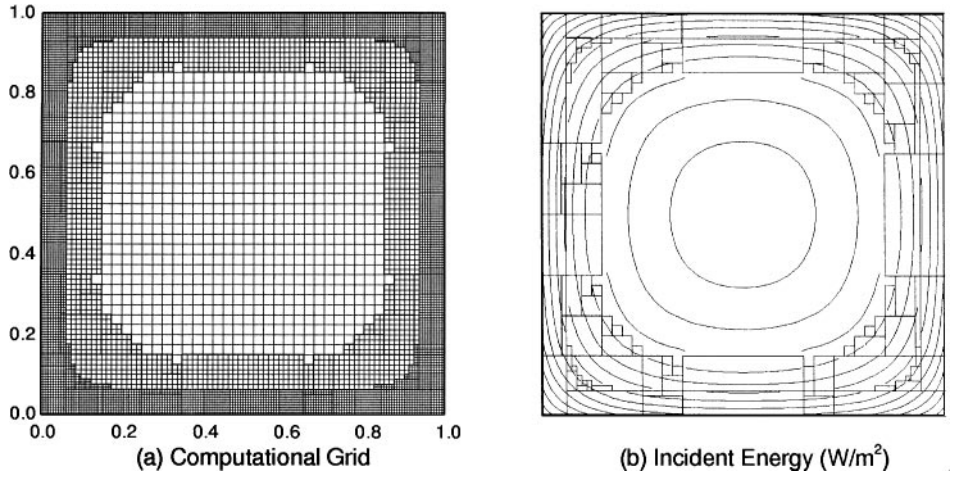

FIG. 2. Refined grid and solution for Case 1 ($\kappa = 1, \theta = 0.05$).

using less than half the cells of the uniform grid. Howell and Bell [14] observed similar trends with respect to CPU time and memory requirements for the adaptive solution of the incompressible Navier–Stokes equations. Figures 2 and 3 display the final grid structures and incident energy fields for optical thicknesses of 1 and 10, respectively. An error tolerance (θ) of 0.05 was used to generate the results. As seen in these figures, the grid adapts to the steep gradients in the solution. Four levels of refinement are shown.

Convergence characteristics are measured by comparing the number of iterations required for convergence from the adaptive algorithm to that of the single grid algorithm. A range of absorption coefficients and wall emissivities is considered. The single and multiple-level grids used in the study correspond to the 40×40 uniform mesh and the final adaptive meshes for $\theta = 0.05$, respectively. The number of refinement levels for the adaptive algorithm was constrained to four (although some conditions do not require four levels), and the number of iterations corresponds to the last refinement cycle. Table 2 displays the results. For the case of

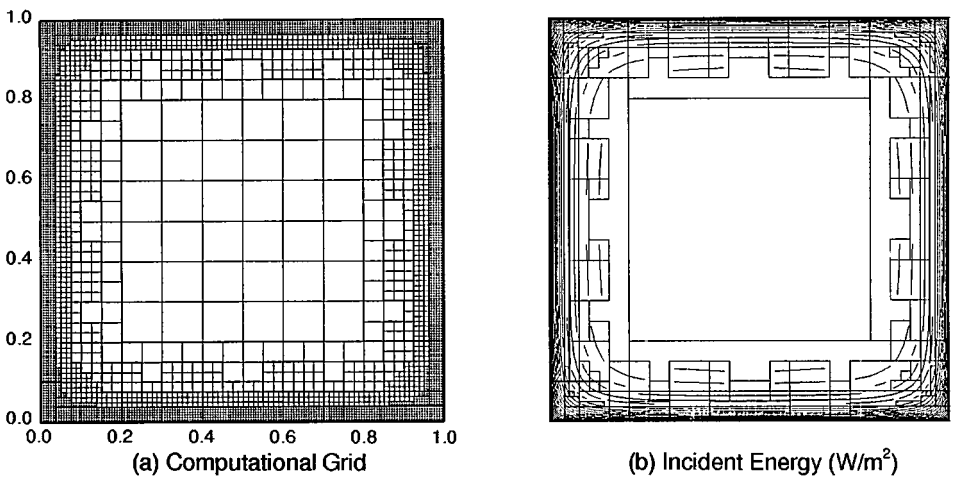

FIG. 3. Refined grid and solution for Case 1 ($\kappa = 10, \theta = 0.05$).

TABLE 2
Convergence Characteristics for Case 1 (Iterations for Convergence)

	$\varepsilon = 0.1$		$\varepsilon = 0.5$		$\varepsilon = 1.0$	
κ	SG	AMR	SG	AMR	SG	AMR
0.1	63	62	19	19	1	5
1	17	17	11	10	1	5
10	10	8	8	8	1	5

Note. SG = single grid algorithm; AMR = adaptive mesh algorithm.

black walls, convergence is degraded slightly by the multiple-level algorithm; however, for the gray cases, convergence is comparable. When the walls are gray, convergence is governed by the explicit treatment of the reflected boundary rays, rather than by any communication delay caused by the multiple-level algorithm. For some conditions, the convergence of the multiple-level algorithm is actually better than the single-grid algorithm.

4.2. *Rectangular Enclosure with a Purely Scattering Medium*

The second case consists of a square enclosure with black walls and an isotopically scattering medium. The lower wall has an emissive power of unity, and the other walls have zero emissive power. All walls of the enclosure have an emissivity of 1. The case has been analyzed by a number of workers [10, 11, 15] and serves as a good benchmark for scattering applications.

Because exact solutions are not available to this problem, the accuracy may not be quantified exactly. To compensate, the SD error is measured by comparing DO results to those from a 320×320 uniform grid and the second-order CLAM scheme (see Ref. [12]). This solution is taken as the benchmark to which all other solutions are compared using the error norms of Eqs. (17) and (18).

The case was analyzed on both uniform and adaptive grids. For the adaptive analyses, the local intensity in the denominator of the error estimator (Eq. (12)) was replaced by the blackbody intensity at the lower wall because of negligibly small radiant intensities in a portion of the domain. Error and timing results are shown in Table 3. As displayed

TABLE 3
Error and Timing Statistics for Case 2 (σ = 5)

Grid	$\|E\|_1$	$\|E\|_\infty$	CPU time (s)	No. of cells
20×20	6.243	28.54	11.74	400
40×40	3.313	16.29	47.22	1600
80×80	1.756	10.32	195.56	6400
$\theta = 0.05$	5.724	26.42	39.83	652 (2)[a]
$\theta = 0.025$	3.344	15.13	135.5	1948 (3)
$\theta = 0.01$	1.459	13.79	775.9	11220 (4)

[a] Value in parentheses denotes final number of refinement levels.

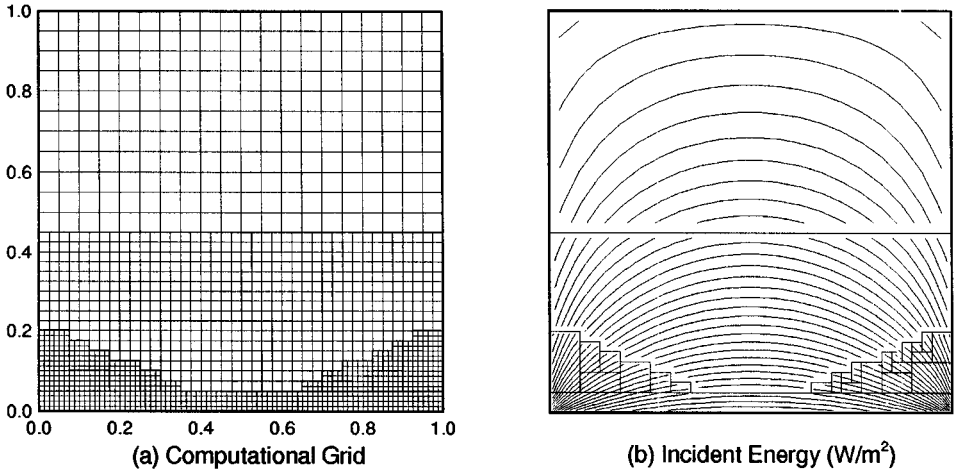

FIG. 4. Refined grid and solution for Case 2 ($\sigma = 5, \theta = 0.025$).

in the table, the adaptive algorithm consistently requires more CPU time and more cells to achieve a given error level compared to the single grid algorithm. The primary reason for these results is again the lack of disparate length scales in the benchmark problem; the algorithm refines a large percentage of the domain. Figure 4 displays the final adapted grid structure and the resulting incident energy field. High gradients are visible near the lower wall which has the driving emissive power. Outlines of the grid structure are overlaid on the incident energy contour.

Convergence characteristics for the single and multiple-level algorithms are shown in Table 4. A range of scattering coefficients and wall emissivities is considered. The single and multiple-level grids used in the study correspond the 40×40 uniform mesh and the final adaptive meshes for $\theta = 0.05$, respectively. The number of refinement levels for the adaptive algorithm was constrained to four, and the number of iterations corresponds to the last refinement cycle. The table indicates that the convergence is generally not affected by a multiple-level algorithm. The explicitly treated in-scattering and reflection terms dominate the convergence. For some conditions, the multiple-level algorithm requires fewer iterations. Although they were not applied here, mesh rebalance techniques [16] may be used to accelerate convergence for problems with significant scattering. Such acceleration techniques will likely prove effective for the multiple-level grid structure and should be investigated in future work.

TABLE 4
Convergence Characteristics for Case 2 (Iterations for Convergence)

	$\varepsilon = 0.5$		$\varepsilon = 0.75$		$\varepsilon = 1.0$	
σ	SG	AMR	SG	AMR	SG	AMR
0.1	20	20	12	12	7	7
1	43	38	27	22	19	17
10	327	257	258	199	223	169

Note. SG = single grid algorithm; AMR = adaptive mesh algorithm.

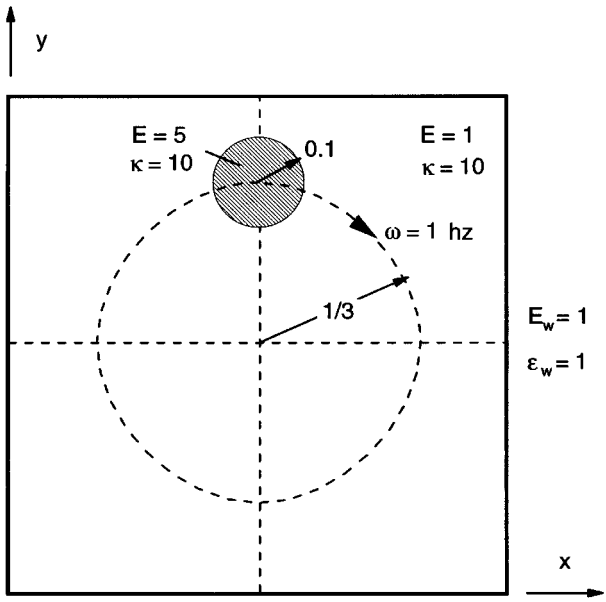

FIG. 5. Geometry and conditions for Case 3.

4.3. *Black Enclosure with Time-Varying Emission*

Radiative transfer is considered in a rectangular enclosure with a moving area source. The case was selected to conceptually simulate a moving flame front in a combustion analysis and to illustrate the adaption process. The conditions are displayed in Fig. 5. A circular area of radius 0.1 and emissive power of 5 moves in a path of radius 1/3 and origin located in the center of the enclosure. The emissive power of the surrounding media and walls is unity, the absorption coefficient (κ) of the entire domain is 10, and the walls are black. The "spot" moves at a frequency of 1 rotation per second.

Figure 6 displays the adapted grids and predicted incident energy fields at four times in the rotation cycle—$t = 0$, 0.125, 0.25, and 0.375 s. These results were generated with an error tolerance (θ) of 0.05, a 20×20 base grid (level 0), and with the number of refinement levels constrained to three. At each timestep, four adaption cycles were allowed. As shown in Fig. 6, the algorithm adapts the grid to the area of high emission and captures the steep gradients in the solution. The incident energy is high in the vicinity of the source and decays as rays penetrate the surrounding media. Rotational symmetry of 90° may be seen by comparing the results which differ by a 0.25 s time interval (e.g., results at $t = 0$ and $t = 0.25$ s).

To illustrate the efficiency gains of the AMR algorithm, error and timings statistics were compiled at time $t = 0.375$ s for the single grid algorithm with a number of uniform discretizations and for the AMR algorithm with error tolerances of 0.1 and 0.05. The results are shown in Table 5 and are graphically displayed in Fig. 7. The error was based on a benchmark solution obtained from a uniform 320×320 grid with the second-order CLAM scheme [12]. The listed CPU time reflects the time of the final refinement cycle, a consideration based on the transient nature of the problem. As seen in the table, the AMR algorithm requires approximately 75% less CPU time than the single grid algorithm to reduce the maximum error to <4% (compare $\theta = 0.05$ and 160×160 results). The

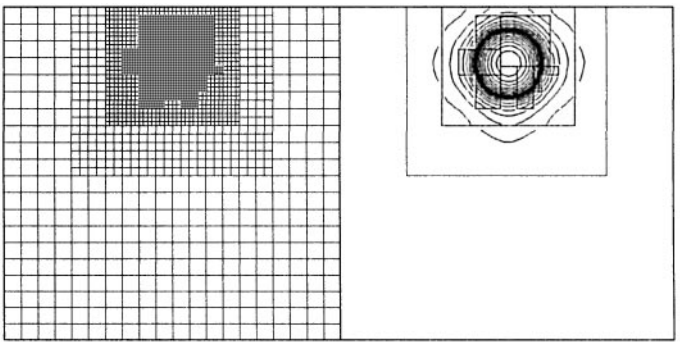

(a) t = 0.0 s

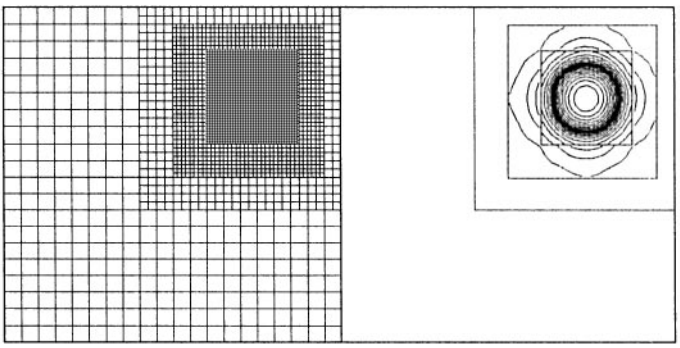

(b) t = 0.125 s

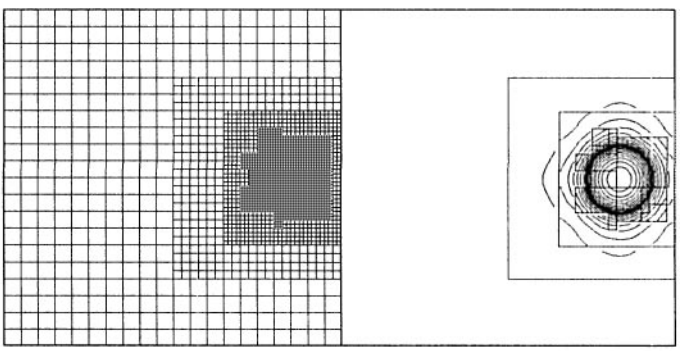

(c) t = 0.25 s

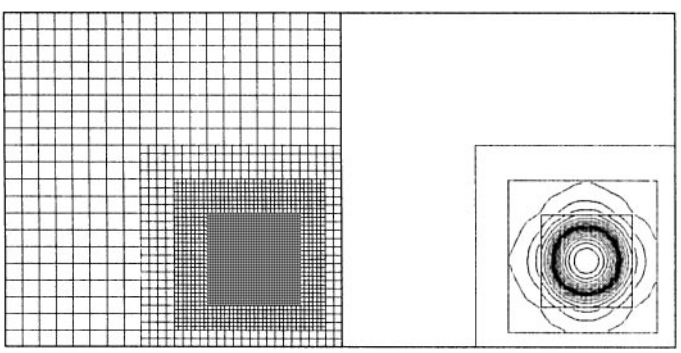

(d) t = 0.375 s

FIG. 6. Refined grid (left) and predicted incident energy (right) for Case 3($\theta = 0.05$).

TABLE 5
Error and Timing Statistics for Case 3 (t = 0.375 s)

Grid	$\|E\|_\infty$	CPU time (s)	No. of cells
40×40	23.8	1.09	1600
80×80	11.4	4.47	6400
160×160	3.61	18.6	25600
$\theta = 0.1$	11.4	1.31	1200 (2)[a]
$\theta = 0.05$	3.61	4.32	4188 (3)

[a] Value in parentheses denotes final number of refinement levels.

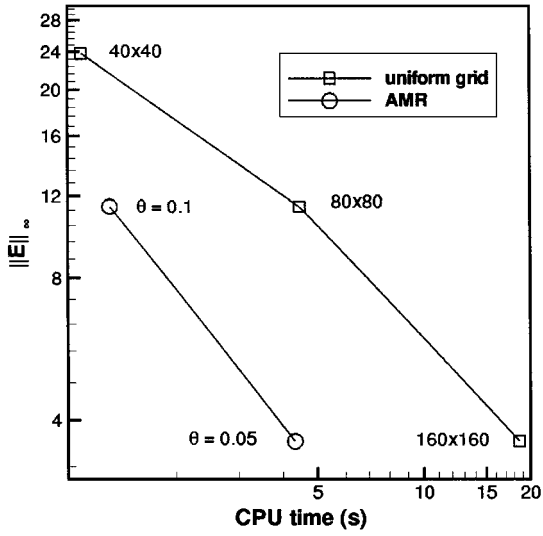

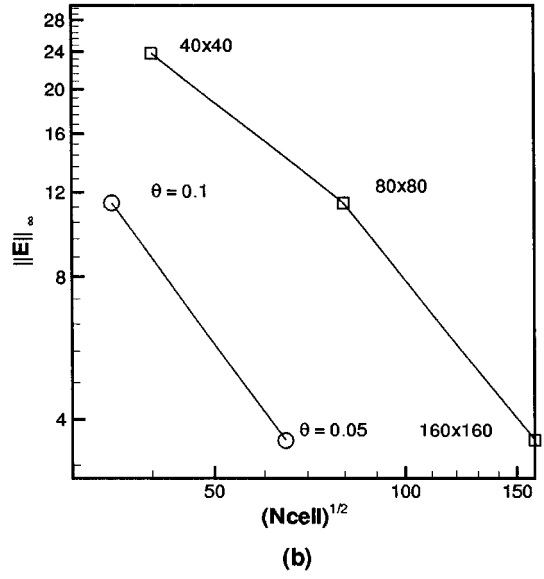

FIG. 7. Error for Case 3 as a function of (a) CPU time and (b) number of cells ($t = 0.375$ s).

maximum errors for the adapted grids are identical to those of the uniform grids that match the resolution of the finest refinement level, indicating that the adaptive algorithm is appropriately refining the regions of increased error. For example, the most refined region for the $\theta = 0.05$ adaptive analysis has the same resolution as the uniform 160×160 grid. In addition, the AMR algorithm reduces the number of cells by an even greater factor than the CPU time, $\sim 84\%$. These improved results, compared to those of the previous two cases, may be attributed to the local nature of the problem—the length scale of the region of elevated emissive power is somewhat smaller than the scale of the problem domain. This attribute is shared by many physical problems of engineering importance. In combustion problems, for example, regions of elevated emissive power (temperature) are usually confined to a small portion of the domain, and high gradients of emissive power are generally confined to the even smaller region of the flame sheet. As a consequence, the AMR algorithm may be expected to provide similarly significant CPU time and memory reductions when applied to physical combustion problems.

5. SUMMARY

An adaptive mesh refinement algorithm has been formulated and implemented for the discrete ordinates method. The resulting algorithm has exhibited convergence characteristics comparable to those of the single grid algorithm. In addition, the algorithm has illustrated the ability to adapt to areas of high local truncation error, based on a simple error estimator. For the two basic benchmark cases considered, the AMR algorithm did not show any efficiency gains over the single grid algorithm. This anomaly is attributed to the nature of the benchmark problems—large areas of uniform emissive power. In contrast, the last problem, with its range of length scales, clearly demonstrated the ability of the AMR algorithm to reduce both computation time and memory requirements. This case also illustrated adaption to a moving front and provides a prelude to integrating the radiation algorithm into a transient, reacting flow code, a research effort which is currently underway.

APPENDIX A: EXACT SOLUTION TO CASE 1

The exact solution to the discrete ordinates equation is

$$I_m(x, y) = \left(I^o - I_b\right)e^{-\kappa s} + I_b, \tag{A1}$$

where

$$s = \min\left(\frac{x - x^o}{\mu_m}, \frac{y - y^o}{\xi_m}\right) \tag{A2}$$

and

$$x^o = \begin{cases} 0, & \mu_m > 0 \\ X_L, & \mu_m < 0; \end{cases} \qquad y^o = \begin{cases} 0, & \xi_m > 0, \\ Y_L, & \xi_m < 0. \end{cases} \tag{A3}$$

The incident energy from the exact spatial solution of the DO equations may be found by

forming the angular quadrature of the above intensity expression:

$$G(x, y) = \sum_{m=1}^{M} w_m \, I_m(x, y). \tag{A4}$$

APPENDIX B: NOMENCLATURE

C	set of ordered grids
E	error, %
G	incident energy, W/m^2
I	intensity, W/m^2 · sr
L	transport operator
M	total number of discrete ordinates directions
N_{cell}	number of control volumes in computation mesh
N^l	number of rectangular grids in level l
$\boldsymbol{n}$	surface normal
$\boldsymbol{P}$	projection operator
$\boldsymbol{r}$	position vector, m
R	residual
s	path length, m
S	source term, W/m^3-sr
S_n	order of discrete ordinates approximation
t	time, s
V	volume, m^3
w_k	direction weights
x, y	coordinate directions, m
β	extinction coefficient ($=\kappa+\sigma$), m^{-1}
Γ	domain boundary
ε	emissivity
θ	error tolerance
κ	absorption coefficient, m^{-1}
Λ	spatial domain
$\partial\Lambda$	domain boundary
μ, ξ, η	direction cosines
ρ	reflectivity ($=1-\varepsilon$)
σ	scattering coefficient, m^{-1}
Ω	direction with direction cosines (μ, ξ, η)

Superscripts

e	external
in	internal
l	level
$l_{\max}$	finest refinement level
n	iteration
o	reference

Subscripts

m	direction
b	blackbody
i, j	nodal indices
k	generic index
n	n^{th} S_n approximation

Miscellaneous

$'$	incoming direction
bold	vectorial quantity
–	exact value, average value
$\langle\cdot\rangle$	spatial averaging operator
$\|\|\cdot\|\|$	norm

ACKNOWLEDGMENTS

This work was supported by the Applied Mathematical Sciences Program and the HPCC Grand Challenge Program of the U.S. DOE Office of Mathematics, Information, and Computational Sciences under Contract DE-AC03-76SF00098. Additional support was provided by the Applied Mathematical Sciences Program of the U.S. DOE Office of Mathematics, Information, and Computational Sciences under Subcontract 3643100.

REFERENCES

1. J. Bell, M. Berger, J. Saltzman, and M. Welcome, *SIAM J. Sci. Comput.* **15**(1), 127 (1994).
2. L. Fuchs, *Comput. Fluids* **14**, 69 (1986).
3. Y. Kallinderis, *Int. J. Numer. Methods Fluids* **15**, 193 (1992).
4. W. A. Fiveland and A. S. Jamaluddin, *J. Thermophys. Heat Transfer* **5**(3), 335 (1991).
5. W. A. Fiveland, *J. Thermophys. Heat Transfer* **2**(4), 309 (1988).
6. E. E. Lewis and W. F. Miller, *Computational Methods of Neutron Transport* (Wiley, New York, 1984).
7. M. F. Modest, *Radiative Heat Transfer* (McGraw–Hill, New York, 1993).
8. W. A. Fiveland, *ASME HTD* **72**, 89 (1991).
9. M. J. Berger and P. Colella, *J. Comput. Phys.* **83**, 64 (1989).
10. W. A. Fiveland, *Trans. ASME, J. Heat Transfer* **106**, 699 (1984).
11. W. A. Fiveland and J. P. Jessee, *J. Thermophys. Heat Transfer* **9**(1), 47 (1995).
12. J. P. Jessee and W. A. Fiveland, *ASME Proceedings of the 31st National Heat Transfer Conference, Houston, TX, August 3–6*, p. 133 (1996).
13. O. C. Zienkiewicz and J. Z. Zhu, *Int. J. Num. Meth. Eng.* **24**, 337 (1987).
14. L. H. Howell and J. B. Bell, *SIAM J. Sci. Comput.*, to appear (1997).
15. A. C. Ratzel and J. Howell, *J. Heat Transfer* **105**, (1983).
16. W. A. Fiveland and J. P. Jessee, *J. Thermophys. Heat Transfer* **10**(3), 445 (1996).